

See discussions, stats, and author profiles for this publication at: <https://www.researchgate.net/publication/331451623>

Topological phases in acoustic and mechanical systems

Article · March 2019

DOI: 10.1038/s42254-019-0030-x

CITATIONS

41

READS

2,095

3 authors:



Guancong Ma

Hong Kong Baptist University

33 PUBLICATIONS 2,214 CITATIONS

[SEE PROFILE](#)



Meng Xiao

Wuhan University

97 PUBLICATIONS 1,747 CITATIONS

[SEE PROFILE](#)



Che Ting Chan

The Hong Kong University of Science and Technology

387 PUBLICATIONS 16,725 CITATIONS

[SEE PROFILE](#)

Some of the authors of this publication are also working on these related projects:



Meta Materials [View project](#)



topological photonics [View project](#)

Topological phases in acoustic and mechanical systems

Guancong Ma^{1,4*}, Meng Xiao^{2,4*} and C. T. Chan^{3*}

Abstract | The study of classical wave physics has been reinvigorated by incorporating the concept of the geometric phase, which has its roots in optics, and topological notions that were previously explored in condensed matter physics. Recently, sound waves and a variety of mechanical systems have emerged as excellent platforms that exemplify the universality and diversity of topological phases. In this Review, we introduce the essential physical concepts that underpin various classes of topological phenomena realized in acoustic and mechanical systems: Dirac points, the quantum Hall, quantum spin Hall and valley Hall effects, Floquet topological phases, 3D gapless states and Weyl crystals.

Weyl points

Point degeneracies on the band structure, with local properties describable by the Weyl Hamiltonian. They can be regarded mathematically as a magnetic monopole in momentum space.

Fermi arcs

In classical wave crystals, a type of isofrequency cut present as arcs in the momentum space. In condensed matter physics, the cut of eigen-spectra is at the Fermi energy.

Sound and mechanical vibrations are ubiquitous. Their study dates to antiquity, and they can be characterized by Newtonian or Lagrangian mechanics, which are at the core of classical physics. Surprisingly, exciting new discoveries in acoustics and mechanics continue to emerge. In the early 1990s, by drawing an analogy to the quantum theory of solids, physicists showed with theory^{1,2}, observation³ and experimentation⁴ that acoustic and elastic waves propagating through a periodic array of scatterers exhibit frequency regimes in which the waves cease to propagate, analogous to the electronic bandgaps in semiconductors. The study of such periodic acoustic or mechanical systems, dubbed phononic crystals, has now matured into an exciting research field. In recent years, fuelled by the discovery of topologically non-trivial phases in electronic systems (in particular, topological insulators) and their counterparts in photonic systems⁵, phononic crystals have rapidly become a setting for studying new physics and exotic phenomena related to topological phases.

Topology is an important tool that has not been fully utilized in traditional band theories. It describes the global properties of wavefunctions over an entire band and is robust against local perturbations, preserving certain symmetries, unless the perturbation is strong enough to close the gaps between bands. Topology offers a deep understanding of the phenomena associated with acoustic and mechanical systems, understanding that cannot be obtained by numerically solving Newtonian or Lagrangian equations. Topological concepts also give new paradigms for designing devices with improved functionalities. Such possibilities have fuelled interest in the emerging fields of topological acoustics and topological mechanics.

In this Review, we outline the basic concept of the geometric phase and extend it to periodic acoustic

systems in which topological notions emerge. We focus on 1D phononic crystals and showcase the physical implications of Zak phases and topological transitions that can arise in such systems. We then discuss topological phases in 2D systems in detail. We discuss the formation of Dirac points in phononic crystals and then discuss various mechanisms to introduce topological phases. Finally, we discuss topological phases in 3D systems, as exemplified by the recent realization of Weyl points and Fermi arcs in phononic crystals.

Geometric phase

The geometric phase was first proposed in 1956 by Pancharatnam for the propagation of light through a sequence of polarizers⁶, and was later generalized by Berry for quantum mechanics⁷. The geometric phase is a universal concept that emerges in the adiabatic cyclic evolution of any state in a system. A familiar example is the Foucault pendulum. The swinging plane of the pendulum rotates by an angle (a phase shift) because of the rotation of the Earth, which carries the pendulum in an adiabatic cyclic motion⁸ (BOX 1). Many phenomena in classical mechanics can be attributed to the geometric phase, which offers a deep connection that links many superficially unrelated phenomena.

In analogy to the Berry phase of linearly polarized light propagating along a helical optical fibre⁹, it was shown in 2012 that the geometric phase can also emerge for transverse elastic vibrations propagating along a spring¹⁰. Intuitively, any transverse wave with linear polarization can be viewed as the superposition of two circularly polarized waves with opposite polarization, and therefore the transverse wave carries a spin degree of freedom (circular polarization). The spin degree of freedom can be represented on the Poincaré sphere, and an adiabatic process along a closed loop on the Poincaré

¹Department of Physics, Hong Kong Baptist University, Kowloon Tong, Hong Kong, China.

²Key Laboratory of Artificial Micro- and Nano-structures of Ministry of Education and School of Physics and Technology, Wuhan University, Wuhan, China.

³Department of Physics, Hong Kong University of Science and Technology, Clear Water Bay, Hong Kong, China.

⁴These authors contributed equally: Guancong Ma, Meng Xiao.

*e-mail: phgcma@hkbu.edu.hk; phmxiao@whu.edu.cn; phchan@ust.hk
<https://doi.org/10.1038/s42254-019-0030-x>

Key points

- Acoustic and mechanical systems are versatile platforms to study a wide range of topological phases that were first investigated in condensed matter physics.
- Topological phenomena that can be observed include Dirac points and analogues of the quantum Hall effect, quantum spin Hall effect, valley Hall effect, Floquet topological phases, gapless states and Weyl systems.
- Because classical acoustic systems are different from condensed matter systems (for example, they lack Kramers degeneracy), new approaches are needed to realize topological phases.
- Schemes of symmetry breaking in phononic crystals play a key role in the realization of these topological phases, and their consequences and limitations are discussed.

sphere defines the geometric phase. Surprisingly, such a spin-redirection geometric phase is also manifested in sound, a longitudinal scalar wave that lacks a spin degree of freedom. Yet, a similar geometric phase effect can be observed, thanks to the existence of intrinsic orbital angular momentum (OAM) in the form of a sound vortex¹¹ (BOX 1). The sound vortex example shows that adiabatic evolutions in real space can induce the geometric phase in reciprocal space, analogous to the spin-redirection phase observed in light propagating in a helical optical fibre.

Geometric phase in phononic crystals

A geometric phase can also emerge in the adiabatic evolution of a state in other types of parameter spaces, including in the reciprocal space of a periodic system. In such a system, the change in wavevector k drives the state along its band. For any path that remains on the same band and does not intersect with any other band, evolution along this path is adiabatic, and the geometric phase is well defined. Owing to the periodicity of the reciprocal space, the evolution is also cyclic when the wavevector traverses the entire Brillouin zone.

We start our discussion by considering the Su–Schrieffer–Heeger (SSH) model¹², which has been used to describe conductive and semiconductive polymers. The model consists of a 1D chain of atoms with periodically alternating hopping parameters, t and s , between nearest neighbours (FIG. 1a). The unit cell for the 1D chain is chosen so that s is the inter-cell hopping and the unit cell has inversion symmetry with respect to its centre. The Hamiltonian matrix can be written as

$$H = \begin{pmatrix} 0 & \varepsilon \\ \varepsilon^* & 0 \end{pmatrix} \quad (1)$$

where $\varepsilon = t + se^{-ik}$ and k is the Bloch wavenumber. Tuning $|t/s|$ can open or close the bandgap. For $|t/s| \neq 1$, the system has a bandgap; for $|t/s| = 1$, the gap closes at the Brillouin zone edge (FIG. 1b).

The acoustic analogue of the SSH chain has been experimentally realized with a coupled resonator system¹³ (FIG. 1c). Each atomic site is mimicked by an acoustic resonator, which carries resonant sound modes that are the counterparts of atomic orbitals. Hopping between acoustic resonators is realized by joining neighbouring resonators with small tubes. The hopping strength is tunable by adjusting the cross-sectional areas of the tubes.

The acoustic SSH system offers the convenience of in situ examination of wavefunctions, which is extremely difficult in electronic systems. Such examination reveals that at the Brillouin zone edge, if $|t/s| \neq 1$, the wavefunction of one band is symmetric with respect to the inversion centre of the unit cell, while the other is anti-symmetric. In addition, these two bands are inverted upon crossing the gap-closing point $|t/s| = 1$. The evolution of the bulk band symmetry can be characterized by the Zak phase ϑ , which is the geometric phase defined for isolated bulk bands for 1D periodic systems¹⁴. Thanks to the periodicity, each branch in the 1D band structure can be knitted together at the Brillouin zone edge to form a closed loop. In this case, the Zak phase is computed by integrating the Berry connection over the Brillouin zone. Owing to the inversion symmetry of the unit cell, the Zak phase has quantized values of 0 or π ¹⁴, and it undergoes a transition from 0 to π (or from π to 0) when the system is driven across the gap-closing point. The Bloch wavefunctions of an acoustic SSH chain are shown in FIG. 1d. When a band has $\vartheta = \pi$, the state switches symmetry when evolved from the lower to higher band edge (equivalent to evolving from $k=0$ to $k=\pi/a$, where a is the lattice constant). When $\vartheta=0$, the symmetry of the state remains unchanged in the same process.

The geometric property of the bulk bands also manifests in properties at the surface, where localized modes can emerge. From the viewpoint of wave physics, surface impedance is a determining factor for the existence of modes localized at the edge of or the interface between phononic crystals or photonic crystals. A natural question arises of whether a link can be established between the surface impedance and the geometric phase of the bulk bands. Such a link has been established for an AB-layered photonic crystal¹⁵. This link is important for several reasons. First, with the geometric phase of bulk bands determined, the surface impedance can be controlled^{16–18}. Second, the bulk geometric phase involves all the eigenstates on a band and is hence difficult to measure. The link between the easily measured surface impedance and bulk geometric phase hence provides a feasible way to determine bulk properties through the surface impedance. Third, the topological notion of bulk–edge correspondence, which predicts the existence of boundary modes using bulk topological characteristics, becomes more heuristically transparent if the topological characteristics (Zak phase) can be directly associated with classical wave parameters (surface impedance).

The Zak phase in an acoustic system has been measured in a 1D phononic crystal that can be regarded as the continuous-wave extension of the SSH model. The phononic crystal is a cylindrical waveguide with periodically alternating cross-sectional areas¹⁹. The modulation in cross-sectional area induces an impedance mismatch between adjacent sections, which gives rise to Bloch scattering. Band inversion can be realized by adjusting the length difference between cross sections with different areas while keeping the lattice constant unchanged. The band Zak phases were determined by direct measurement of the wavefunction symmetry at the Brillouin zone centre and edge. The Zak phase

Adiabatic cyclic evolution

A cyclic change in a parameter that is slow enough that the physical system remains in its instantaneous eigenstate, the eigenvalue of which is not degenerate with any other eigenvalue of the Hamiltonian.

Berry phase

A phase difference acquired over an adiabatic cyclic evolution, resulting solely from the geometric properties of the parameter space of the system Hamiltonian.

Poincaré sphere

A graphical representation of all the polarization states of a pure state of light on the surface of a 3D sphere.

Berry connection

The local gauge potential for Berry curvature $\mathbf{A} = i\langle u_R | \nabla_R | u_R \rangle$ is the instantaneous eigenstate of the system with parameter \mathbf{R} . Viewable as a momentum-space analogy to the vector potential for a magnetic field.

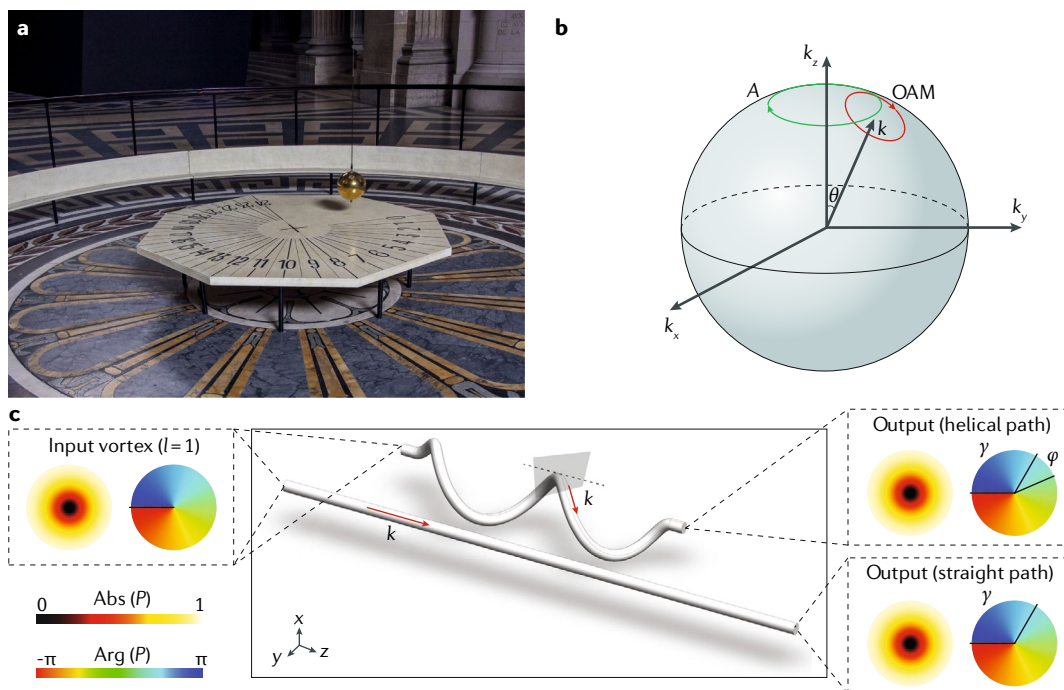
Surface impedance

The surface property of a truncated bulk for waves. For acoustic waves, surface impedance is defined as the ratio of the sound pressure variation to the local fluid velocity.

Box 1 | Geometric phase from adiabatic cyclic evolutions

We introduce the concept of the geometric phase through the example of a Foucault pendulum. A Foucault pendulum, such as the one at the Panthéon, Paris (see the figure, panel a), exhibits precession. The swinging plane of the pendulum is continuously rotating, and a full precession cycle takes approximately 32 hours. This is a consequence of the geometric phase ϕ accumulated by the pendulum as the rotation of the Earth carries it in an adiabatic cyclic motion, which, for the pendulum in Paris, occurs along the latitude line of $48^\circ 52' \text{ N}$. The geometric phase is proportional to the solid angle θ subtended by the curve A (see the figure, panel b).

In acoustics, a beam of sound can carry an intrinsic orbital angular momentum (OAM) when it possesses azimuthal wavevector components, because angular momentum $L = \mathbf{r} \times \mathbf{p}$, where \mathbf{r} is the spatial coordinate with $\mathbf{r} = 0$ at the centre of the beam and \mathbf{p} is the momentum related to the azimuthal wavevectors. For example, for a sound vortex carrying a topological charge $l = 1$ (see the figure, panel c), its cross-sectional pressure (P) amplitude profile has a doughnut shape, and it has one phase dislocation line (the dashed line on the phase map). Such a vortex can be viewed as the superposition of two mutually perpendicular dipolar transverse wave modes with a relative phase of $\pi/2$. When the vortex propagates along a slowly winding helical path, its propagation \mathbf{k} is continuously and adiabatically changing direction to trace the helix. Consequently, the intrinsic OAM rotates as the vortex propagates. This rotation in real space induces a geometric phase in reciprocal space, similar to the spin-redirection phase of light propagating in a chiral optical fibre. This geometric phase manifests as the rotation in the orientation of the vortex by an angle φ . By contrast, the same vortex propagating in a straight waveguide with the same length accumulates only a dynamical phase γ . The rotation of a vortex in 3D (represented by the group $SO(3)$) is non-commutative; therefore, the geometric phase is related to both the sign and the value of the topological charge l . See REF.¹¹ for more details on this topic.



of the second band was determined by comparing the phononic crystal's reflection phases η , which are related to the surface impedance Z through $Z = i \cot(\eta/2)$. By contrast, the reflection wave at a sound-hard surface at the bandgap frequency has zero phase change. Interface states were observed inside the overlapping frequencies of the bandgaps of the phononic crystals, with different Zak phases that meet at the interface. The transition of the Zak phase has subsequently been observed in a variety of 1D systems, such as a granular chain of periodic quartz cylinders²⁰, an elastic beam²¹ and a nanophononic system²². The notion of a Zak phase in 1D systems can also be applied to 2D systems. For a 2D system, a Zak phase can be defined along a 1D band with a fixed wavevector component along a specific direction. The bulk–edge correspondence is valid when the direction is parallel to the boundary, in which case the wavevector

parallel to the boundary is a good quantum number in a truncated system^{23–25}.

Dirac points

Having illustrated the basic concepts with 1D examples, we now discuss topological phases in 2D systems. We start with the graphene lattice. Like the acoustic analogue of the SSH model (FIG. 1c), an ‘acoustic graphene’ can be constructed using a lattice of coupled cylindrical acoustic resonators, in which sound propagates inside cavities (FIG. 2a). The cavity mode with a pressure profile varying only along the cylinder axis can simulate the behaviour of the out-of-plane p orbital in graphene. The system simulates the behaviours of graphene at low-energy excitations. The band structure (FIG. 2b) exhibits linear dispersion along the KT and KM directions near K, with double degeneracy at the K point, and

Good quantum number

The eigenvalue of an operator that remains unchanged as the system evolves. In the example in the main text, the system changes from a boundary-less periodic system to a truncated bulk.

Berry curvature

A local gauge field defined as $\Omega = \nabla \times \mathbf{A}$, where \mathbf{A} is the Berry connection.

similarly for K' . The band structure can be fitted with a simple tight-binding model with only nearest-neighbour hopping²⁶ (FIG. 2b). Two fitting parameters are used: the on-site energy and the hopping strength. The full band structure calculated with the tight-binding model

(FIG. 2c) reveals that there are two conical dispersions, called Dirac cones, around the K and K' points (FIG. 2d). To lowest order, the Hamiltonian around the Dirac point can be written as²⁶

$$H(\mathbf{q}) = q_x \sigma_x + \tau q_y \sigma_y \quad (2)$$

where σ_x and σ_y are the Pauli matrices and q_x and q_y are the wavevector components measured from the K ($\tau = 1$) and K' ($\tau = -1$) points, where τ represents the valley index.

The Dirac cone dispersion is a consequence of the lattice symmetry and is protected by the time-reversal symmetry and the inversion symmetry of the honeycomb lattice. The Berry curvature is an even function of k if the system has space inversion symmetry and an odd function of k if it has time-reversal symmetry; hence, the Berry flux vanishes everywhere inside the Brillouin zone of a system with both time-reversal symmetry and inversion symmetry for nondegenerate points²⁶. However, the Berry phase along any loop encircling the Dirac cone is π ²⁶, which can lead to anti-localization²⁹, meaning that a small amount of disorder can increase transport rather than impede it. Because the Berry phases along any loops around the Dirac cone are the same, the Dirac point itself possesses a quantum π of Berry flux. Breaking either time-reversal symmetry or inversion symmetry lifts the degeneracy at the Dirac point (K or K') and opens a gap (FIG. 2d). However, the Berry flux is still localized around the K and K' points after the symmetry breaking.

The Dirac cone degeneracy can also be lifted without breaking inversion symmetry or time-reversal symmetry by annihilating two Dirac cones. By applying uniaxial tensile strain along the ΓM direction, the Dirac cone can be shifted along the KM direction²⁸. When the strain is large enough, two Dirac cones annihilate each other at the M point, and a bandgap opens. The required strain is calculated to be extremely large for graphene²⁸. However, such a topological transition can be observed in an analogue of the graphene lattice in soft materials²⁴. The topological transition can be characterized by the change in Zak phases and induces a surface state localized between two domains that lie in the parameter regions before and after the transition. It has also been shown that a specific strain field in a graphene lattice can be regarded as a gauge potential that leads to a pseudo-magnetic field^{29,30}. Applying such a strain field in a graphene analogue can lead to the realization of Landau quantization for classical waves^{31,32}.

Other phenomena resulting from the dispersion of the Dirac cone are also observed in analogues of graphene^{33–42}. The dispersion of Dirac cones has been measured in different systems^{35,36}. In one experiment³⁵, an acoustic wave propagates on the surface of a plastic slab containing a graphene lattice of cylindrical boreholes (FIG. 2e). The acoustic wave is excited by a loudspeaker, and the field distribution, including phase information, is measured by a microphone. The dispersion is then retrieved from the phase information. The transport of acoustic waves near the Dirac point can be well approximated by the Dirac equation. Owing to the conservation

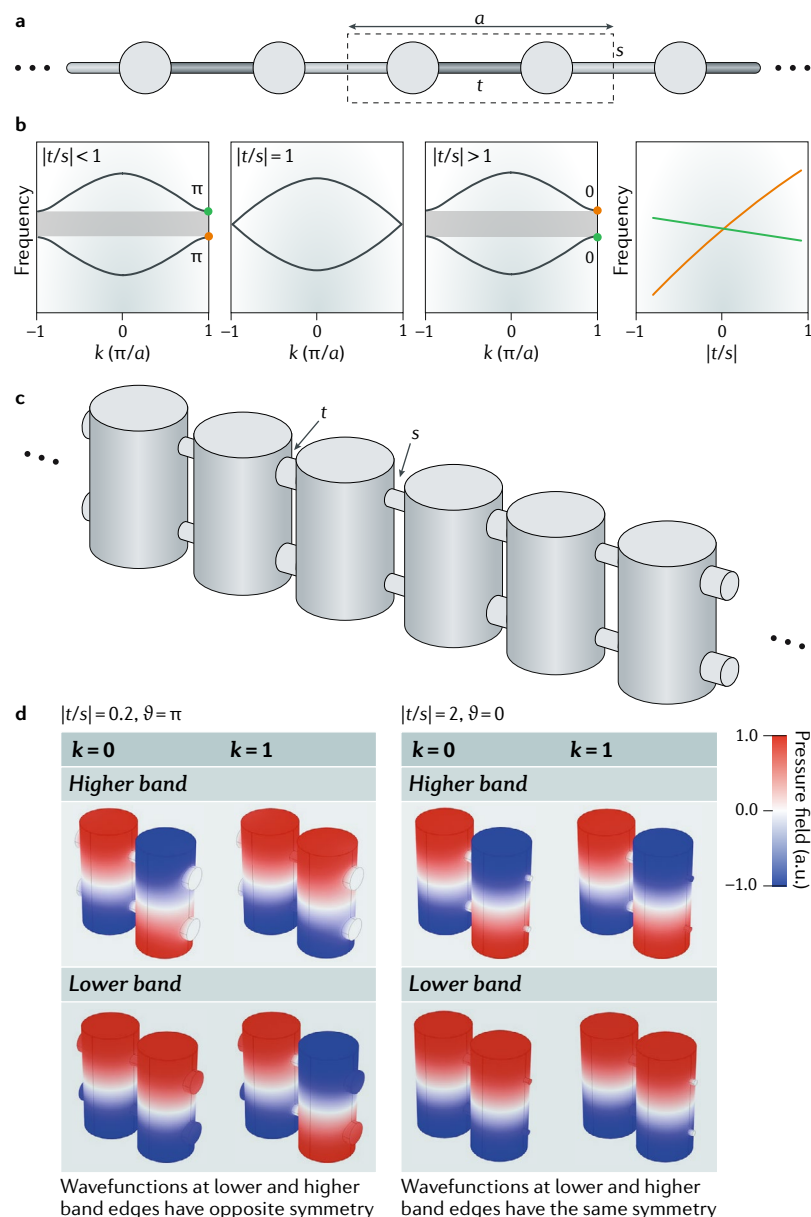


Fig. 1 | Geometric phase in a 1D phononic crystal. **a** | Schematic of a dimerized molecule chain, a 1D periodic system with period a . Circles represent the molecules, and lines represent the coupling parameters t and s . **b** | The molecular chain can be described by the Su–Schrieffer–Heeger (SSH) model, which displays a gap when $|t/s| \neq 1$. By tuning the coupling constants, the gap closes at the edge of the Brillouin zone at $|t/s| = 1$. This is a topological transition point, characterized by a change in the Zak phase ϑ for both bands. The frequencies of the two relevant bands at the edge of the Brillouin zone depend on $|t/s|$ (as shown in the right-most panel). **c** | Realization of the SSH chain with acoustic cavities. Each cylinder represents an acoustic ‘molecule’, and cavities are coupled by connecting tubes, with coupling constants t and s . **d** | Simulated Bloch wavefunctions for the two bands shown in panel **b** at the lower and higher band edges, which correspond to the Brillouin zone centre ($k=0$) and Brillouin zone edge ($k=1$, in units of π/a). For $\vartheta = \pi$, the wavefunction of a band switches symmetry type as the Bloch wavenumber k increases; for $\vartheta = 0$, the symmetry type remains unchanged across the band. a.u., arbitrary units.

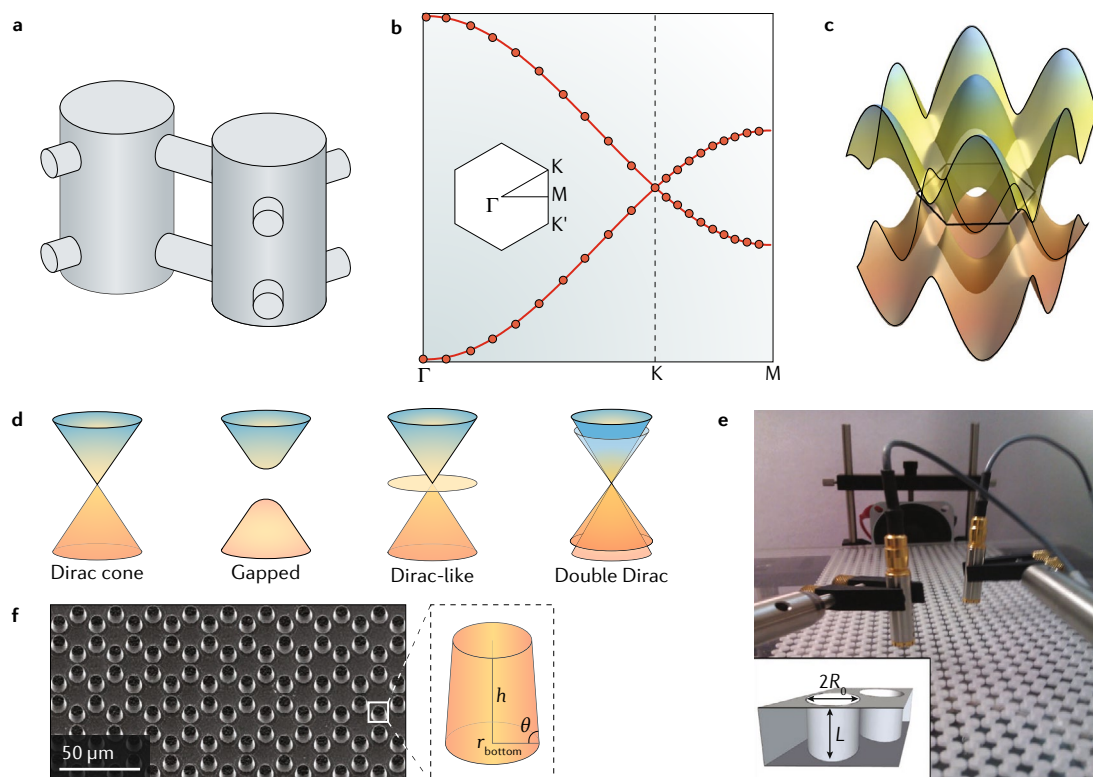


Fig. 2 | Dirac cone dispersion. **a** | A unit cell used in simulations of an acoustic analogue of graphene. The system consists of resonance cavities forming a hexagonal lattice. The cavities simulate the atoms, and the connection tubes between cavities simulate hopping among them. The cavities are made of sound-hard boundaries and are filled with air. **b** | Band structure of the acoustic graphene in panel **a**. The dots are data from full-wave simulations, and the curves come from a tight-binding model with on-site energy and nearest-neighbour hopping strength as the only fitting parameters. The inset of panel **b** shows the first Brillouin zone. **c** | 3D band structure from the tight-binding model showing conical dispersion at the K and K' points. **d** | Linear dispersion resulting in the formation of a Dirac cone; modified dispersion giving rise to the appearance of a gap when the degeneracy of the two linearly intersecting bands is lifted; a Dirac-like cone; and a double Dirac cone. **e** | Experimental realization of acoustic graphene, consisting of a plate with a lattice of cylindrical holes of radius R_0 and depth L (inset). Waves are excited by a loudspeaker, and two microphones are used to measure the propagating waves. **f** | Experimental realization of phononic graphene, consisting of a hexagonal lattice of truncated cones defined by base radius r_{bottom} , height h and angle θ (inset). Panel **e** is adapted with permission from REF.³⁵, APS. Panel **f** is adapted from REF.³⁷, Springer Nature Limited.

of flux, the transmission of a phononic crystal slab for k near the Dirac cone is inversely proportional to the thickness of the slab³³. This anomalous transport behaviour was experimentally verified in acoustic graphene³⁴. Dirac quasiparticle-like transport of surface elastic waves has been demonstrated on a substrate decorated with an artificial phononic graphene³⁷ (FIG. 2f). Analogues of graphene in elastic waves have also been investigated in both linear^{40,41} and nonlinear⁴² systems.

Quantum Hall effect

In quantum mechanics, a 2D electron gas in an out-of-plane uniform magnetic field has energy levels that are quantized into highly degenerate bands known as Landau levels. If the 2D electron gas has a finite size, the Landau levels bend up and become dispersive near the edges of the sample. At the edges where the Landau levels intersect with the Fermi level, the system becomes a conductor with quantized conductivity (FIG. 3a). This is known as the integer quantum Hall effect. An intuitive way to understand this phenomenon is to

consider the cyclotron motion of the electrons (FIG. 3a). Because the magnetic field breaks time-reversal symmetry in the system, the electrons can orbit in only one direction. When the system is finite, the cyclotron orbits must break at the system edge, and the electrons have no choice but to skip to the next orbit, thereby forming a one-way flow of current that is immune to backscattering. Thouless and others showed that in a quantum Hall system with a periodic potential, each energy band can be labelled with an integer number that represents the topological invariant⁴³. This number became known as the Thouless–Kohomoto–Nightingale–den Nijs (TKNN) number, and later as the band Chern number C . The quantum Hall effect was observed in graphene^{44,45} soon after it was first synthesized, because graphene is an excellent host of a 2D electron gas. The theory of the quantum Hall effect was subsequently extended to photonic systems⁴⁶. Like electronic systems, photonic systems require a static magnetic field to break time-reversal symmetry^{44,46–48}. Breaking time-reversal symmetry in a hexagonal lattice induces a total Berry flux π localized

around K and K'; hence, the total Berry flux through each band is 2π , and the Chern number is 1.

However, acoustic and elastic waves are magnetically inert. Achieving an analogue of the quantum Hall effect — which requires broken time-reversal symmetry — demands new approaches. In acoustics, one way to break time-reversal symmetry is to set the wave-sustaining medium in constant motion. It was shown that the vorticity field around a vortex in an irrotational fluid can induce an effect similar to the Aharonov–Bohm effect, which causes a dislocation in the wavefront of a sound passing through it⁴⁹. An alternative approach to break time-reversal symmetry is to use a resonator with air circulation to achieve non-reciprocity for the realization of an acoustic isolator⁵⁰. The air flow is an external bias that breaks time-reversal symmetry for sound waves that propagate in the system.

The same strategy can be employed to break time-reversal symmetry in phononic crystals (FIG. 3b).

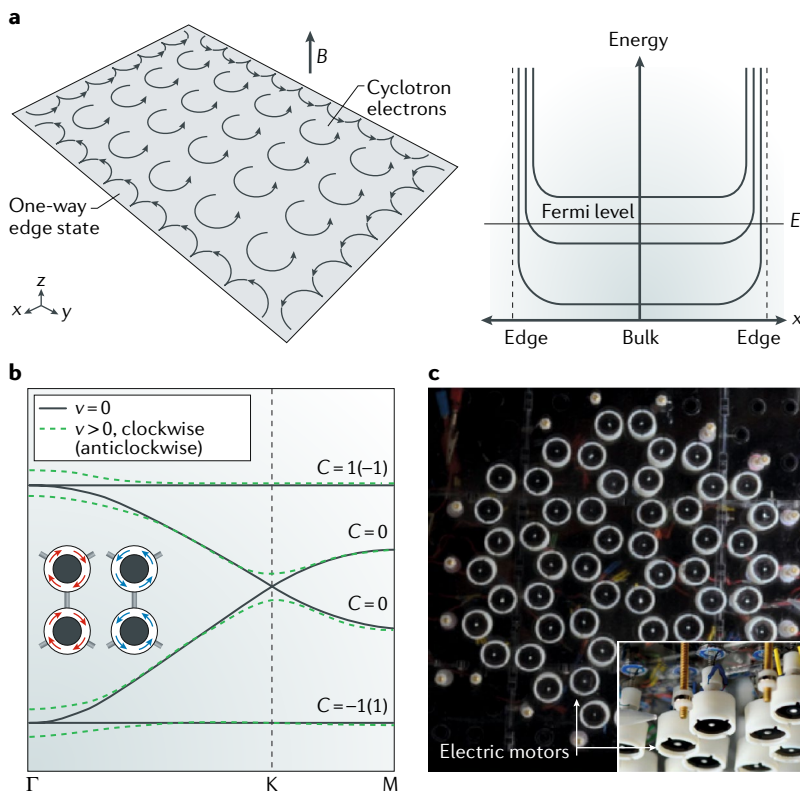


Fig. 3 | Breaking time-reversal symmetry. **a** | The quantum Hall effect arises when, in an out-of-plane magnetic field B , the cyclotron orbits (shown in the left image) of a 2D electron gas are quantized to discrete levels, known as the Landau levels (shown in the right image). These levels become dispersive near the edge of the system, forming one-way conductive channels. An effective magnetic field can be emulated in acoustic or mechanical systems by introducing rotation in unison in each unit cell to break time-reversal symmetry. **b** | Breaking time-reversal symmetry opens a gap at the Dirac point, and the resulting isolated bands can each be labelled with a Chern number C , characterizing their topology. We show acoustic graphene, with each unit cell consisting of two identical ring-shaped resonators (inset). Its band structure is plotted using black curves. The dashed curves show the band structure when the filling medium of the resonator is circulating. **c** | A similar strategy has been employed to achieve topological non-trivial states in a mechanical network, in which the time-reversal symmetry is broken by the spinning of 'atoms', that is, electric motors. E_F , Fermi energy; v , velocity. Panel **b** is adapted from REF.⁵³, CC-BY-4.0. Panel **c** is adapted with permission from REF.⁶⁰, PNAS.

Several theoretical studies have shown that in a 2D phononic crystal that possesses a Dirac cone, when the fluid within each unit cell is set in a unidirectional rotation, time-reversal symmetry is broken, lifting the degeneracy at the Dirac point and opening a bandgap^{51–54}. If the two bands above and below the gap are isolated, the Chern number of the band can be calculated by integrating for each band the Berry curvature over the entire Brillouin zone. The non-zero Chern number reveals that the bands are topologically non-trivial. The number of interface states is determined by the sum of the Chern numbers for all bulk bands below the bandgap under consideration; this sum defines the gap Chern number. When the phononic crystal is truncated by a normal reflective surface such as a sound-hard boundary, which is topologically trivial and has a Chern number of zero, surface states emerge at the boundary, as required by the bulk–boundary correspondence^{55,56}. This surface state can be found using a calculation on a strip of unit cells with a finite length, confined with a reflective surface along one direction and periodic along the other direction. Notably, in addition to acoustic graphene, breaking time-reversal symmetry can also induce an acoustic Chern insulator with a Dirac-like point⁵⁷ (BOX 2).

Breaking time-reversal symmetry using rotating media has the advantage that the underlying mechanism is intuitively obvious, but the implementation in practice is often difficult. It has been shown that to achieve a sizeable non-trivial bandgap, a high rotational speed is required, which in turn causes undesirable or complicated effects such as nonlinearity and viscous effects. These issues can make experimental observation of a sizeable bandgap rather challenging. As a result, experimental attempts were non-existent until a recent report on acoustic honeycomb lattice consisting of cavities of a high quality factor, which substantially reduced the required rotational speed⁵⁸. The so-called active liquids approach⁵⁴, which relies on self-propelling particles in the fluid to generate a spontaneous flow, also represents an interesting possibility to overcome these issues.

However, rotating parts, such as gyroscopes or DC motors, are mechanical components that are readily available. Using rotation to break time-reversal symmetry can therefore be realized straightforwardly in mechanical lattices⁵⁹. An example is a mechanical network that is a honeycomb lattice of spring-coupled mass blocks (FIG. 3c). The normal modes of the system are separated into acoustic and optical branches, which are characterized by in-phase and anti-phase oscillations, respectively. The branches join at a Dirac point. For certain lattice configurations, when all mass blocks are replaced by DC motors that rotate in the same direction (see the inset, FIG. 3c), the global time-reversal symmetry is broken, and a region of low density of states emerges between the acoustic and optical branches. This region is populated only by modes that are localized to the edge of the system, which can be used for one-way propagation of vibration that is immune to defects⁶⁰. In another approach, it was predicted that the centrifugal force on a rotating 2D honeycomb network of spring-coupled masses can

Kramers pairs

In time-reversal-symmetric systems with half-integer total spins, every energy eigenstate is at least two-fold degenerate. This degeneracy is protected by time-reversal symmetry, and the two eigenstates form a Kramers pair.

be treated as a uniform effective magnetic field, thereby giving rise to a topologically non-trivial state⁶¹.

Quantum spin Hall effects

Spin-orbit coupling in graphene can open a gap at the Dirac point, and the two bands are topologically non-trivial. The system can be regarded as two copies of a quantum Hall system in which spin-up and spin-down electrons feel opposite magnetic fields. Finite-size systems support two dispersive edge states with opposite propagation directions, each populated by electrons with opposite spin⁶². The propagation is robust and cannot be backscattered unless the spin is flipped, for example, by

magnetic impurities. This phenomenon, the quantum spin Hall (QSH) effect, was observed in semiconductor heterostructures with strong spin-orbit coupling^{63,64}. In a QSH system, time-reversal symmetry is intact. Thanks to the intrinsic spin-1/2 of electrons, time-reversal symmetry guarantees that electronic states are two-fold degenerate at the time-reversal-invariant points, with Kramers pairs comprising spin-up and spin-down states. Spin-orbit coupling splits the bulk degeneracy away from these time-reversal-invariant points and introduces opposite gauge fields for spin-up and spin-down states. The degeneracies between edge states at time-reversal-invariant points are still preserved.

At first glance, it is surprising that the QSH effect can have a classical counterpart. The time-reversal operation for fermions satisfies $\mathcal{T}^2 = -1$, with \mathcal{T} being the time-reversal operator. By contrast, neither photons nor phonons form Kramers pairs, because $\mathcal{T}^2 = 1$ for such systems. However, careful analysis shows that a crucial characteristic for the QSH effect is the two-fold degeneracy of states, which is a result of time-reversal symmetry. Therefore, to realize the equivalent of the QSH effect in classical systems, the key step is to construct a pseudospin system in which the two pseudospin states can emulate Kramers pairs, that is, be time-reversal counterparts of each other. Note that compared with the Dirac Hamiltonian, which can also be written in Pauli matrices and can therefore also be named pseudospin-1/2, the requirement of time-reversal pairs is an important additional constraint.

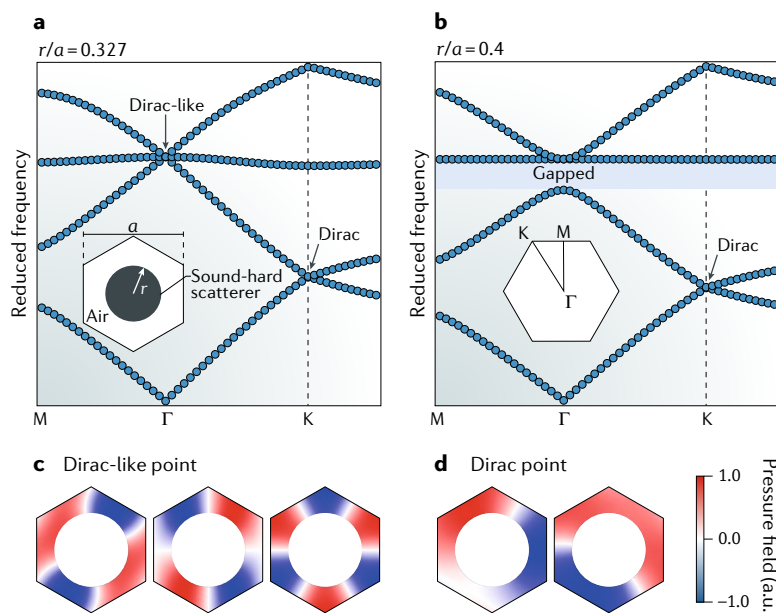
To construct such states in a periodic system is no easy task. The first realization of the QSH effect in a mechanical system was made in an intricate lattice of pendulums⁶⁵. The dynamics of such a system is governed by Newton's equation $(\omega^2 + D)x = 0$ for a harmonic mode with angular frequency ω , displacement x and dynamical matrix D . On the basis of the similarity with the Schrödinger equation $(E - H)\psi = 0$ for a quantum state ψ with energy E and Hamiltonian H , the goal was to design a system with D sharing the form of the Hamiltonian of a QSH system. The QSH Hamiltonian was obtained for a model consisting of two independent copies of a Hofstadter model⁶⁶ on the square lattice with opposite flux per plaquette. Through a local basis rotation, this complex QSH Hamiltonian can be made real and be implemented using spring connections as coupling terms. To emulate the spin degree of freedom in a QSH system, each lattice site consists of two pendulums, which form a local Kramers pair.

For continuous systems, an analogue of the QSH effect for sound (FIG. 4) has been studied in 2D honeycomb arrays of metallic rods in a background of air⁶⁷. Double Dirac cones, which contain two dipole modes and two quadrupole modes, exist at the Brillouin zone centre thanks to accidental degeneracy. A gap can be opened from the double Dirac cones by tuning the ratio of rod radius r to lattice constant a (the filling ratio). The two double bands above and below the gap are either dipole or quadrupole bands (FIG. 4a). At the interface between two phononic crystals, one with a filling ratio above the value at the gap-closing point and the other below, these modes hybridize by the forming of a pair

Box 2 | Dirac points and Dirac-like points

The existence of a Dirac point is the consequence of both time-reversal and inversion symmetry of the crystal lattice. However, through the fine-tuning of microstructures, a point with similar linear dispersions and degeneracy, called a Dirac-like point, can also occur at the Γ point in a phononic crystal through the mechanism of accidental degeneracy (note that the existence of a Dirac-like point still requires time-reversal symmetry to hold⁵⁷). This can be seen in a phononic crystal that supports both Dirac and Dirac-like points (see the figure inset, panel a). In such a system, the Dirac point at K survives the change in parameter (radius r of the sound-hard scatterer), whereas the Dirac-like point at Γ occurs only for $r/a = 0.327$, where a is the lattice constant (see the figure, panels a and b). Compared with the Dirac point at K, the Dirac-like point is a triply degenerate point — which enables its use as a pseudospin-1 system¹³³ — with a flat band intersecting the conical dispersion at Γ . Their eigenfields are shown in the figure, panels c and d. The Dirac-like point at the Γ point gives rise to zero-index metamaterials, in which the effective mass density or the effective compressibility, or both, is zero^{134–138}. A Dirac-like cone can be used as a pseudospin-1 system¹³³, thanks to its triple degeneracy. Another important point is that the Berry phase is π along any path that encloses a Dirac point. By contrast, encircling a Dirac-like point yields a zero Berry phase¹³⁷. Dirac-like conical dispersions have been extensively discussed for both acoustic and elastic waves^{135,137,139–142}.

In addition to the Dirac-like cone dispersion, other conical dispersions exist, such as the semi-Dirac cone¹⁴³, which can be constructed by the accidental degeneracy of eigenmodes from different representations of the symmetry group possessed by the system¹⁴⁴. Of these, the double Dirac cones (FIG. 2d) draw special attention^{145,146} because lifting the four-fold degeneracy in a suitable way leads to the analogue of quantum spin Hall systems in classical scalar wave systems¹⁴⁷.



a.u., arbitrary units.

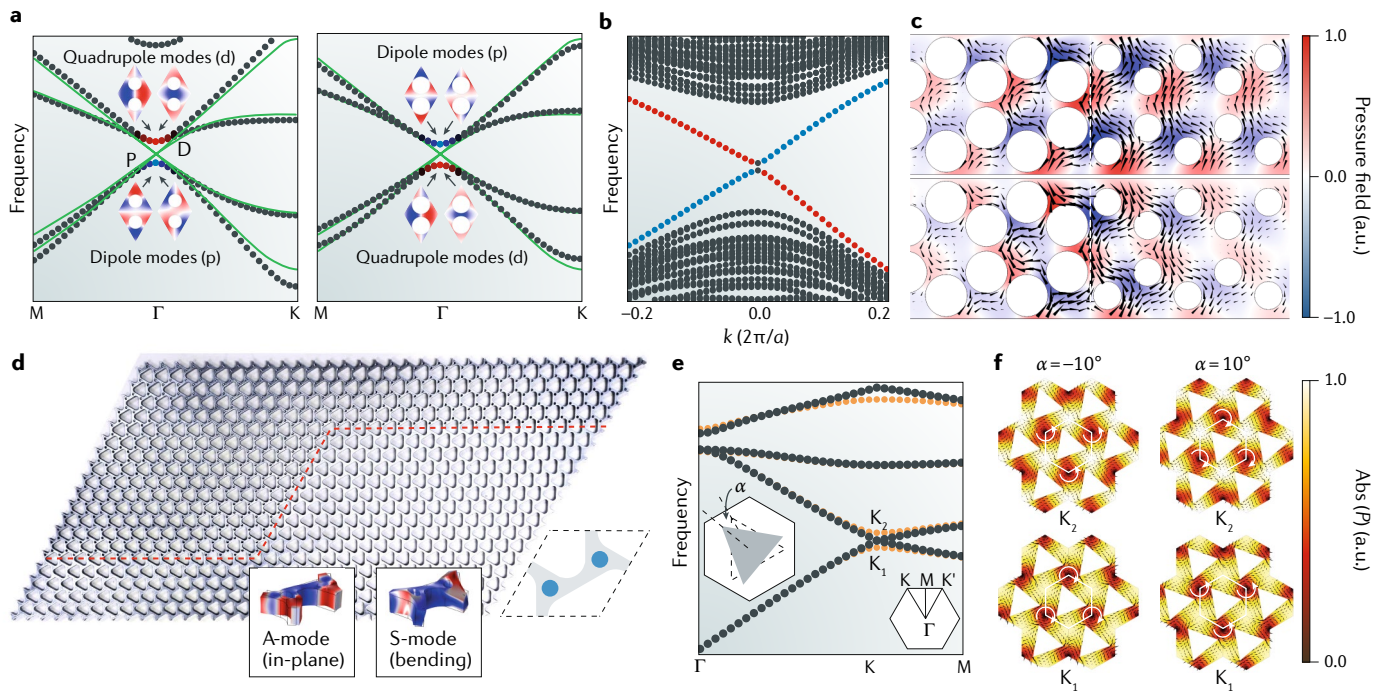


Fig. 4 | Acoustic and mechanical analogues of the quantum spin Hall effect and valley Hall effect. **a** | At a specific intermediate ratio of cylinder radius to lattice constant, a 2D honeycomb lattice of sound-hard cylindrical scatterers exhibits double Dirac cones (solid curves) owing to accidental degeneracy. If the ratio is decreased (as shown in the left image) or increased (as shown in the right image), a bandgap opens, sandwiched by two double bands that touch at Γ (black dots). The insets show the quadrupole and dipole modes. Band inversion occurs when the ratio of cylinder radius to lattice constant crosses the gap-closing point. **b** | At the interface of two different phononic crystals, each with a ratio of cylinder radius to lattice constant at one side of the gap-closing point, two states are localized (coloured dots), one with the pseudospin up and the other with the pseudospin down. Black dotted lines represent bulk energy bands. **c** | Away from $k=0$, the wavefunctions of the interface states are counter-spinning vortices, owing to the hybridization of the dipole and the quadrupole modes. They constitute the pseudospins in this system. The interface is marked by the dashed line. **d** | In a patterned plate with holes (unit cell in inset), the symmetric (S)-modes and antisymmetric (A)-modes of Lamb waves (insets) can hybridize to form pseudospins. **e** | Rotation of the triangular scatterer in a triangular lattice by a small angle α (inset) breaks the C_{3v} symmetry and opens a gap at K and K' (first Brillouin zone shown in inset), leading to two extrema known as valleys, indicated by the points K_1 and K_2 . Black dots show the band structure at $\alpha=0$; orange dots show the band structure at finite α . **f** | Wavefunctions at the valleys of an array of rotated triangular scatterers (shown in panel **e**) consist of acoustic vortices, which play the role of valley pseudospins for the acoustic realization of valley Hall transport. White arrows indicate the sense of rotation of the vortices. The colour scheme for fields in panels **a**, **c** and **d** is indicated by the colour bar in panel **c**. In panels **c** and **f**, black arrows represent time-averaged acoustic Poynting vectors. a , lattice constant; a.u., arbitrary units; k , wavevector; P , pressure. Panel **d** is adapted from REF.⁷⁸, CC-BY-4.0.

of acoustic vortices carrying opposite OAM (FIG. 4c). The vortices are the time-reversal counterparts of each other, thereby satisfying Kramers' theorem, and are the pseudospins of the system. The two pseudospins are associated with net flows of acoustic flux along the interface with opposite group velocity, giving rise to two interface states (FIG. 4b). From the bulk–boundary correspondence^{55,56}, it is known that the system undergoes band inversion when the filling ratio is tuned. Indeed, the spin-Chern numbers of the bands are zero for small r/a and ± 1 for large r/a . Note that because the pseudospins are well defined only at the Brillouin zone centre, the spin-Chern numbers are calculated using an effective Hamiltonian instead of the pseudospin wavefunctions. In the experiment, the interface was excited by a source from one boundary of the phononic crystal to impose a predominant propagation direction. This guarantees that only one type of pseudospin is excited, because the pseudospins are locked to one of the two interface

branches with opposite group velocities. In general, it is difficult to flip the charge of a vortex state in scattering events; therefore, the transport of a so-called chiral spin current of sound is immune to backscattering. Note here that the surface supports surface states propagating along both directions but with different pseudospins. If a sound source was located in the middle of the interface, it would be necessary for the source to selectively excite only one type of pseudospin to achieve one-way transport along the interface. Otherwise, both pseudospins can be excited, and the sound can propagate along the interface in both directions.

A Brillouin-zone-folding scheme for photonic crystals has been proposed in which a honeycomb lattice of rhombic primitive unit cells is treated as a triangular lattice of hexagonal unit cells⁶⁸. In doing so, the Dirac cones at the Brillouin zone corners K and K' fold back to the Brillouin zone centre Γ , forming a double Dirac cone with two dipole modes and two quadrupole

Hofstadter model

A mathematical model describing the behaviour of electrons in a magnetic field in a 2D lattice. The energy levels form a fractal set.

modes. The hybridization of these modes gives rise to vortex states, which satisfy the requirement of Kramers degeneracy. The double Dirac cones are opened by a lattice deformation that breaks the primitive unit cell while maintaining the hexagonal unit cell and C_{6v} lattice symmetry. Band inversion and a topological transition are induced by tuning the geometric parameter of the deformation. This idea was numerically confirmed for phononic crystals⁶⁹. Prior to this zone-folding scheme, double Dirac cones at Brillouin zone corners mimicking Kramers pairs were typically produced using the so-called artificial duality symmetry, which is difficult to achieve in optical systems. The zone-folding scheme makes Kramers-like degeneracy feasible for all kinds of waves, including acoustic and mechanical waves. For example, the idea can be realized in sound at subwavelength scales using a metamaterial crystal consisting of a honeycomb lattice of soda cans, acting as subwavelength Helmholtz resonators for airborne sound⁷⁰. Ring-shaped resonators can sustain degenerate eigenmodes that are essentially two waves propagating in opposite directions^{71,72}. These two modes can also play the role of the pseudospins for acoustics⁷³. These systems are also referred to as Floquet topological insulators in the literature, as discussed below.

As mentioned, achieving the analogue of the QSH effect in classical waves relies on engineering wavefunctions to realize artificial Kramers pairs. These pseudospins can mix with each other through scattering if the underlying symmetry that protects the pseudospin is not preserved at the scattering site. Therefore, one-way transport not only relies on the successful excitation of these states — which can be difficult to achieve — but also is robust against only a certain class of symmetry-preserving scatterers. The same issue also exists for classical wave systems that give rise to the valley Hall effect, which is discussed below.

Similar ideas can be applied to elastic wave systems^{74–76}. For example, the evolution of vortex pseudospin states in the topological interface of two elastic wave phononic crystals has been demonstrated. However, elastic wave systems carry additional degrees of freedom, namely, polarizations, which can also be used to construct pseudospins through polarization hybridization. For example, it has been proposed to realize double Dirac cones in a thin plate this way⁷⁷, using subwavelength microstructures on a plate that also hosts a wavelength-scale triangular lattice. The triangular lattice naturally sustains Dirac cones. However, a thin plate can sustain Lamb modes with distinct vibration patterns that can be regarded as polarizations. Specifically, S-modes involve symmetric vibration about the central plane of the plate and are predominantly longitudinal vibrations; A-modes are antisymmetric bending vibrations of the plate (FIG. 4d, inset). Therefore, two separate sets of Dirac cones exist, each for one vibrational mode. The subwavelength microstructures tune the two Dirac cones to coincide in the formation of double Dirac cones. The hybridization of breathing and flexural vibration near the double Dirac point leads to elastic pseudospins, which also take the form of two counter-rotating vortex-like states. This idea was subsequently realized⁷⁸

in an experiment that used a simplified design (FIG. 4d) in which holes in a plate were used to tune the Dirac points of two vibration modes. Another proposal has been made to realize double Dirac cones in granular graphene consisting of metal beads in contact with each other⁷⁹, for which the on-site mode is the rotational vibration of the beads, and hopping is provided by the friction between contacting beads. The rotational vibrations of the beads are used as pseudospins.

Valley Hall effect

So far, we have considered the topology defined for an entire band. However, this is not a necessity. As discussed above, a geometric phase can be defined for any cyclic adiabatic evolution. Instead of following a Bloch state across the entire Brillouin zone, it is possible to follow its adiabatic evolution along any path on a band. This means that topological characteristics can also be locally defined. In this section, we consider the observable consequences of such local topological charges and how they differ from topology defined for the entire band.

A 2D phononic crystal has been built that is a triangular lattice in which each unit cell has one equilateral triangular rod as a scatterer in a background of air⁸⁰. The lattice and the orientation of the scatterers ensure three-fold rotational symmetry. When the scatterers are orientated such that the K and K' points possess C_{3v} symmetry, Dirac cones are found at K and K' (FIG. 4e). However, the lack of inversion symmetry imposes that the wavefunction must be different at K and K'. By rotating the triangular rods by a small angle, C_{3v} symmetry at K and K' is lifted, and gaps open from the Dirac points, such that two extrema appear at the corners of the Brillouin zone. These extrema are called valleys. By integrating the Berry curvature over a small region that contains only one valley extremum, a non-zero topological charge (π Berry flux), called the valley Chern number, is found localized to the valley. However, the band as a whole is topologically trivial because the valleys K and K' (for the same band) carry opposite topological charges, as inversion symmetry is broken and time-reversal symmetry is preserved. The acoustic Poynting vectors at the valley extrema (one for the higher band, the other for the lower band) exhibit acoustic vortices with opposite topological charges. Interestingly, these two vortex states are spatially separated in real space, and they are found at different corners of the Brillouin zone (FIG. 4f)^{80,81}. The difference in chirality at K and K' can also be used for beam splitting⁸². In addition, owing to the characteristics of the wavefunction at K and K', reversing the rotation angle of the triangular rod (or flipping the entire phononic crystal upside-down) is equivalent to interchanging the two vortices at K and K', thereby leading to the inversion of the valley states. As a result, topological transport phenomena, such as one-way interface modes, are observed in the interface system constructed by two phononic crystals with opposite rotational angles for the triangular rods⁸¹.

The flexibility afforded by phononic crystals enables the exploration of additional degrees of freedom that would be difficult to realize in electronic systems.

Duality symmetry

Symmetry such that Maxwell equations of a source-free system are invariant under $\epsilon \rightarrow \mu$, $\mu \rightarrow \epsilon$, $\mathbf{E} \rightarrow \mathbf{B}$ and $\mathbf{B} \rightarrow -\mathbf{E}$, where ϵ is the dielectric constant, μ is the permeability, \mathbf{E} is the electric field and \mathbf{B} is the magnetic field.

Lamb modes

Two types of mode of waves in a solid plate, one symmetric about the plate mid-plane (characterized by breathing vibrations) and one antisymmetric (characterized by bending vibrations).

Poynting vectors

Vector fields representing the direction and amplitude of local energy flow. In acoustics, the vector field is defined as $\mathbf{S} = P\mathbf{v}$, where P is the pressure variation and \mathbf{v} is the local fluid velocity.

For example, stacking together two 2D phononic crystal layers that are coupled in the out-of-plane direction effectively introduces an additional layer degree of freedom⁹⁰. A rich topological phase diagram emerges simply by rotating the scatterers in each layer⁸³, and a layer topological number can be defined to account for the topological phase diagram. It has also been shown that other types of point group symmetry, such as C_4 , can lead to valleys in reciprocal space away from high-symmetry points⁸⁴. A similar interface state is used to engineer a delay line in a different phononic crystal interface system⁸⁵. Other proposals include building a lattice of acoustic resonators with mismatching resonant frequencies⁸⁶. The valley Hall effect can also be realized in elastic wave systems⁸⁷. The properties of elastic materials can be advantageous for additional tunability. For example, inducing a strain field in the elastic network deforms the lattice in ways that lower the lattice symmetry, thereby inducing the valley Hall effect⁸⁸.

Floquet topological phase

Topological concepts can also be associated with the dynamic evolution of states in time. This can be seen in the Floquet system, which is a system with a time-dependent Hamiltonian periodically driven in time, that is, $H(t+T) = H(t)$, where T is the driving period. The evolution of the system over one driving period can be described by the Floquet operator $\mathcal{F}(T) = \mathbb{T}e^{-i\int_0^T H(t)dt}$, where \mathbb{T} is the time-ordering operator. Applying $\mathcal{F}(T)$ drives the system forward one driving cycle, returning it to the same set of eigenmodes⁸⁹. The band structure of a periodically driven system is fundamentally different to that of a static system. For a temporally driven, spatially periodic system, the Floquet eigenvalues, also known as quasi-energies, give rise to a band structure in which Floquet topological phases are observed.

A straightforward way to realize the Floquet topological phase is to rely on temporal modulation of the parameters of a system. For example, a graphene lattice has been proposed, for which each unit cell is a trimer of coupled acoustic resonators. The bulk modulus (or, alternatively, the volume) of the resonator trimer is sequentially modulated in a temporally periodic way. This is equivalent to modulating the on-site part of the static Hamiltonian. The temporal modulation leads to a direct analogue to the Floquet topological insulator and could lift the degeneracy of the static Dirac point, thereby leading to topologically non-trivial bands and edge states that are robust against both spatial disorder and phase disorder of the modulation⁹⁰.

Temporal modulation is sometimes difficult to achieve in experiments. However, in some cases, temporal evolution can be mapped into a higher spatial dimension. For example, for light propagating in a periodic array of waveguides, the propagation direction of which is in the z direction, the continuous translational symmetry in z is broken when the waveguides are all bent into identical helices. Such extra periodicity associated with the wavevector k_z can be treated as an effective time modulation. Floquet topological phases and the k_z -locked one-way edge state can then be observed in the band structure of quasi-energies⁹¹. A similar idea

has been implemented to demonstrate topologically protected bound states in 1D periodically modulated acoustic waveguide systems⁹².

Interestingly, the Floquet effect also provides an alternate conceptual picture for the topological phase realized using phononic crystals constructed from ring-shaped resonators^{73,93}. As mentioned above, the pseudospins in this case are waves propagating in opposite directions, and the waves experience a phase delay as they go through each resonator. This phase delay can emulate periodic temporal evolution. Therefore, the system can be treated as an example of the Floquet topological phase.

3D gapless states and Weyl systems

Weyl points exhibit conical dispersions in a periodic 3D system. At first sight, they appear to be a simple extension of the 2D Dirac cone to 3D periodic lattices. However, there are important differences. The simplest form of Weyl point is described by the Weyl Hamiltonian⁹⁴

$$H(\mathbf{q}) = q_x \sigma_x + q_y \sigma_y + q_z \sigma_z \quad (3)$$

where the q and σ are the wavenumbers and Pauli matrices, respectively. The equifrequency surfaces form concentric spheres, and the radii of these spheres are proportional to the wavevector (FIG. 5a). Unlike the Dirac Hamiltonian in 2D shown in equation 2, the Weyl Hamiltonian contains all the Pauli matrices. As such, 3D Weyl points can survive any local perturbation, such as lattice deformation. By contrast, 2D Dirac points are easily gapped.

Integration of the Berry curvature on a surface enclosing a Weyl point shows that the Weyl point is a monopole for the Berry flux. Such a monopole can be characterized by a topological charge (Chern number). Depending on the sign of the charge, a Weyl point can be either a source or sink of Berry flux. Weyl points can be annihilated only by annihilating oppositely charged pairs. The associated topological charges explain the topological robustness of the degeneracy at the Weyl points. Because Berry curvature is odd under time-reversal symmetry and even under inversion symmetry, it must vanish for a system with both time-reversal and inversion symmetry. Because Weyl points are sources or sinks of Berry flux, the minimum requirement for a system to exhibit a Weyl point is to break either time-reversal or inversion symmetry. This situation is different from that of 2D Dirac points, because breaking either time-reversal or inversion symmetry lifts the degeneracy at the Dirac point. This subtle yet important difference between Dirac points in 2D and Weyl points in 3D also indicates that Weyl points are far more elusive than 2D Dirac points. 2D Dirac points are the consequence of lattice symmetry; therefore, they can emerge in any wave system, including electromagnetic and acoustic systems.

Given the similarity between the Hamiltonian of a Dirac point in 2D and a that of a Weyl point in 3D, a design strategy is to start with a 2D honeycomb lattice, which guarantees the existence of Dirac points at the Brillouin zone corners (K and K'). A term σ_z , proportional to q_z , which lifts the degeneracy at the Dirac

Time-ordering operator

A mathematical representation of a procedure that orders the product of a series of operators according to the time sequence of these operations.

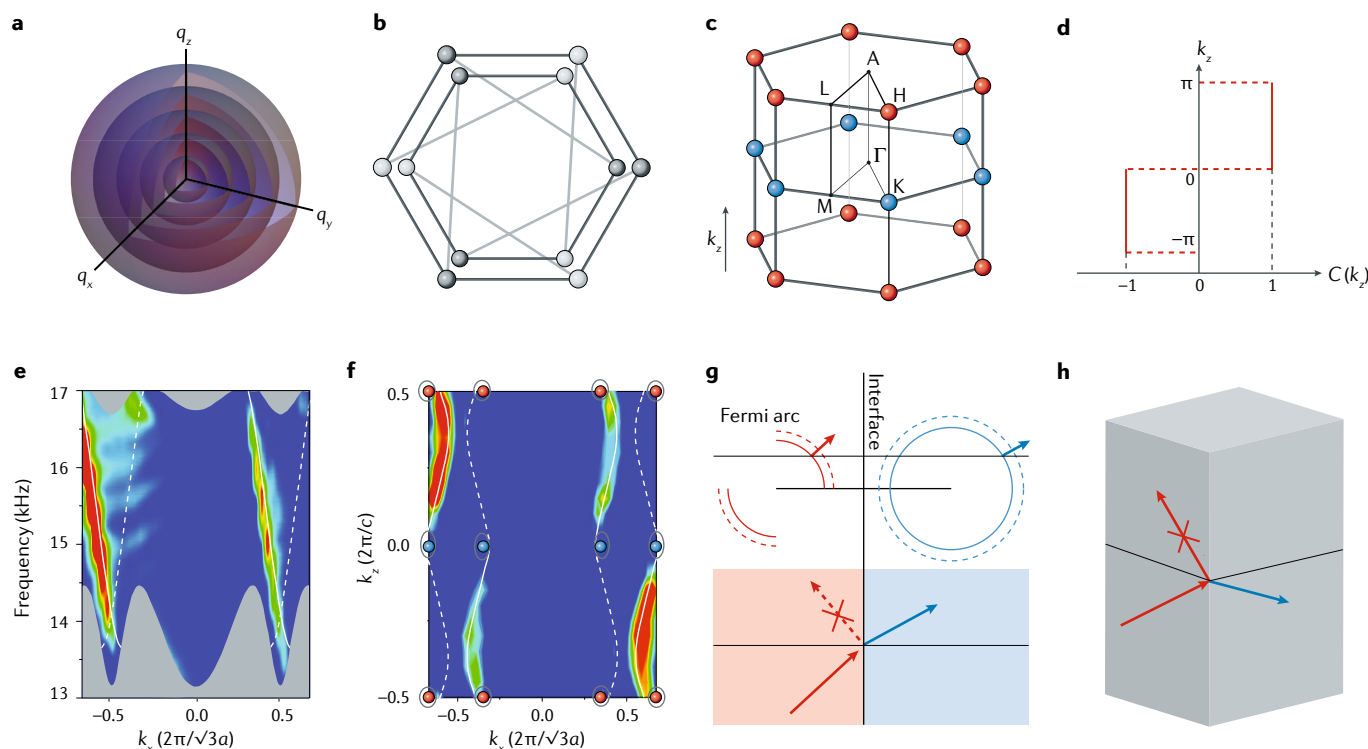


Fig. 5 | Acoustic Weyl semimetal. **a** | Equi-energy surfaces of an isotropic Weyl point. q_x , q_y and q_z are the wavenumbers in the x , y and z directions, respectively. **b** | A tight-binding model based on the two sublattices shown in the schematic exhibits Weyl points in reciprocal space. Dark and light spheres denote the two sublattices of the honeycomb lattice, and dark bonds represent the nearest-neighbour coupling between sublattices. Light bonds represent a next-nearest-neighbour coupling, which is proportional to $k_z \sigma_z$ (k_z is a wavevector, and σ_z is a Pauli matrix) for the Hamiltonian near the points K and K' and the points H and H'. **c** | Weyl point distribution in reciprocal space of the tight-binding model in panel **b**. Blue and red spheres represent Weyl points with topological charges +1 and -1, respectively. **d** | Chern number C for 2D bands with a fixed k_z , for the Weyl point distribution in panel **c**. **e, f** | Surface waves of a chiral phononic crystal. Panel **e** shows the projected band structure at $k_z = 0.5\pi$. Grey areas represent the projection of bulk bands, and dashed and solid white curves represent surface states localized on different surfaces. Panel **f** shows Fermi arcs in the surface Brillouin zone. Spheres represent the projection of Weyl points, solid and dashed lines represent surface arc states localized on different boundaries, and grey ellipses denote the boundary of bulk band projections at 15.4 kHz. **g** | Topological total refraction at an interface between surface arc states and normal surface states. Reflection is forbidden because the Fermi arcs (red open arcs in upper schematic) have no mode for the reflected waves, whereas the transmitted wave is in a trivial state (closed arc in the upper schematic). Solid and dashed curves in the upper schematic represent equal frequency cuts, with arrows pointing towards the higher-frequency direction. **h** | The idea shown in panel **g** can be further exploited to obtain topological negative refraction on the surface of a Weyl semimetal at the edge where two crystal surfaces join. Panels **e** and **f** are adapted from REF.⁹⁹, Springer Nature Limited. Panel **g** is adapted from REF.⁹⁷, Springer Nature Limited.

point⁹⁵, is then added. Such an extension to 3D can be achieved by periodically stacking identical 2D honeycomb lattices in the out-of-plane (z) direction. In a tight-binding model of one such realization (FIG. 5b), nearest-neighbour bonds couple the two sublattices, and next-nearest-neighbour coupling is proportional to $k_z \sigma_z$ for the Hamiltonian near the points K and K' and the points H and H'. Hence, this Hamiltonian exhibits Weyl points at these high-symmetry points (FIG. 5c). Because this tight-binding model preserves C_6 symmetry along the z direction and C_6 preserves the sign of the topological charge, Weyl points on the same k_z plane exhibit the same charge. Alternatively, the $k_z \sigma_z$ term can be introduced using screw symmetry, which can be readily implemented with a three-layer woodpile structure, with each layer rotated by 120° with respect to the layer beneath^{96–98}. These constructions are not the only ways

of generating Weyl points, and in principle, Weyl points may exist in any system with either time-reversal or inversion symmetry, or both, being broken. However, these constructions provide methods to easily locate Weyl points in reciprocal space and hence to exploit the unique properties of a Weyl semimetal.

For a fixed- k_z plane, the total Berry flux passing through it (which defines the Chern number of a 2D band with a fixed k_z) is non-zero (FIG. 5d). The Chern number as a function of k_z changes only at k_z planes that have a net topological charge, because the topological charges of Weyl points play the roles of sinks or sources of Berry flux. The total magnitude of the charge of Weyl points on the $k_z = 0$ and $k_z = \pm\pi$ planes is 2; therefore, the Chern number changes by 2 across these k_z planes. Meanwhile, the system still possesses time-reversal symmetry; therefore, $C(-k_z) = -C(k_z)$. From these two

Screw symmetry

A combination of rotation about an axis and a translation parallel to that axis that leaves a crystal unchanged.

factors, it follows that the Chern number is ± 1 , the sign being determined by the sign of k_z (FIG. 5d). According to the bulk–surface correspondence^{55,56}, a non-zero Chern number indicates the existence of a one-way edge state or states. In a typical band structure for a chiral phononic crystal projected along the k_x direction with a finite k_z (FIG. 5e), a bandgap with a non-zero gap Chern number opens, and one-way surface states emerge inside the bandgap⁹⁹. Here, we consider a stripe of the periodic system, which is finite along the y direction and periodic along the x and z directions (both k_x and k_z are good quantum numbers).

The eigenfrequencies of surface states at different k_x and k_z expand into a 2D surface, and the equifrequency cut of the surface gives a trajectory that is the analogue of a Fermi arc for acoustic waves (FIG. 5f). Acoustic arc surface states were experimentally demonstrated in phononic crystals that implement the tight-binding model shown in FIG. 5b (REFS^{99,100}). Unlike the bulk states or trivial surface states for which a fixed-frequency cut gives a closed contour, for these systems, the arc surface states are pinned to the Weyl points if the frequency is chosen to be the frequency of the Weyl point. Because the arc states are unclosed, it is feasible to design topologically protected transport⁹⁷ (FIG. 5g). A plane wave impinging on the surface can excite only a transmitted wave, because backward modes are absent. This topologically protected transport is consistent with the one-way nature of the surface states at a fixed k_z . To take the idea one step further, the equifrequency contours of the transmission can also be engineered using Fermi arcs, such that the transmitted wave can bend only to the same side of the normal, realizing a form of total negative refraction (FIG. 5h)⁹⁷. An experimental demonstration of this interesting phenomenon has been performed by reflecting surface waves around a corner of Weyl phononic crystals⁹⁷. By carefully engineering the facet of the truncation, the transmitted surface wave can be made to exhibit either positive or negative refraction.

In fact, equation 2 represents only one type of Weyl point (named type I) at which the density of states vanishes. Because a Weyl point is topologically robust, tilting the 3D conical dispersion along an arbitrary direction does not change the topological charge. This tilting operation along, for example, the z direction can be obtained by adding a term $\mu q_z \sigma_0$ to equation 2, where σ_0 is the 2×2 identity matrix, μ determines the tilting strength and only the first order of q_z is included to keep the Weyl point at $\mathbf{q} = 0$. When $|\mu| < 1$, the iso-energy surface near the Weyl point is an ellipsoid; when $|\mu| > 1$, the iso-energy surface near the Weyl point becomes a hyperboloid, and the density of states diverges at the Weyl point as the surface area of the hyperboloid diverges. The density of states remains finite in a periodic system owing to the periodicity of the Brillouin zone. A Weyl point with such a hyperboloid iso-energy surface is a type II Weyl point^{95,101,102}. Type II Weyl points are also different from type I Weyl points in aspects such as their associated surface arc states and Landau levels¹⁰¹.

In addition to the proposed and realized airborne phononic crystal described above, Weyl physics has also been discussed in elastic waves^{103,104}. As a band

degeneracy with topological charge, Weyl points can also possess higher charges^{97,104–106} and include the degeneracy among more than two bands¹⁰⁷. In addition to Weyl points, it has been shown that a nodal surface can also carry non-zero topological charges¹⁰⁸. The nodal surface in REF.¹⁰⁸ is protected by a compound symmetry operator $G_2 = \mathcal{T}\tilde{C}_2$, where \mathcal{T} is the time-reversal operator and \tilde{C}_2 is the two-fold screw symmetry. Such a nodal surface protected by G_2 can be either topologically charged or neutral and can switch between charged and neutral types by emitting or absorbing Weyl points. A charged nodal surface can be realized with an airborne phononic crystal¹⁰⁸.

Like Weyl points, 3D Dirac points can exhibit isotropic linear dispersion¹⁰⁹. Unlike Weyl points, 3D Dirac points include four bands and can be regarded as a combination of two Weyl points with opposite charges. As such, 3D Dirac points are topologically trivial and need to be protected by additional lattice symmetry.

Conclusion and outlook

Topological acoustic and mechanical systems have the advantage of being simple to fabricate and measure. This is in contrast with electronic topological materials, which are limited by the availability of atoms with desirable properties and the need to consider constraints like chemical stability and complexities such as many-body effects. However, acoustic and mechanical systems lack an intrinsic spin degree of freedom and other properties such as Kramers degeneracy, bringing challenges for the realization of topological effects. In the past few years, many groups have overcome these challenges and are now exploring topological concepts to achieve new effects and technological applications. For example, topological interface states may be useful in applications such as sensors and ultrasonic imaging and therapy. The robustness of topological modes is desirable for wave transport applications and may find applications in surface acoustic wave devices.

Parallel to the development of topological waves, it was pointed out that a connection exists between the boundary modes in isostatic lattices (either floppy modes or the state of self-stress) and a winding number for the equilibrium matrix of the isostatic lattices¹¹⁰. For a 1D system of springs connecting a set of masses constrained to rotate at a fixed radius about fixed pivot points, this Hamiltonian is equivalent to that of the SSH model, and hence the winding number characterizing the band topology is equivalent to the quantized Zak phase. The Hamiltonian exhibits intrinsic particle–hole symmetry, which requires the positive and negative eigenvalues of ω to come in pairs. Consequently, the edge modes localized at the domain wall between two domains with different winding numbers must have zero energy. It is then shown that topological notions are useful in characterizing self-stress¹¹¹, buckling states¹¹² and mechanical stability¹¹³ in a myriad of static mechanical systems. More comprehensive accounts of these topics can be found elsewhere^{114,115}.

Emerging ideas are rapidly being applied to classical systems. New concepts such as higher-order topological insulators^{116–120} and topological phases in amorphous

Nodal surface

Two or more states form a nodal surface when they are degenerate over a continuous range of momenta that form a surface in the momentum space.

Isostatic lattices

Lattices consisting of point masses connected by rigid bonds or central-force springs, in which the number of bonds equals the total number of degrees of freedom of the masses.

systems¹²¹ are already realized in mechanical systems. The full potential of many concepts, such as 3D topological insulators^{122,123} and topological Anderson insulators^{124,125}, remains mostly unexplored in the context of classical waves. Even for 1D systems, in addition to the relatively well-known SSH model, models such as the Aubry–André–Harper model^{126,127} and Kitaev model¹²⁸ are drawing interest from wave physicists. The models’

counterparts in phononic systems are becoming important platforms to realize topological effects. In the near future, we believe that the crossover with related research fields in wave physics, such as non-Hermitian wave systems^{129,130} and nonlinear systems^{131,132}, will continue to fuel excitement in this area of research.

Published online: 01 March 2019

1. Sigalas, M. & Economou, E. N. Band structure of elastic waves in two dimensional systems. *Solid State Commun.* **86**, 141–143 (1993).
2. Kushwaha, M. S., Halevi, P., Dobrzynski, L. & Djafari-Rouhani, B. Acoustic band structure of periodic elastic composites. *Phys. Rev. Lett.* **71**, 2022 (1993).
3. Martinez-Sala, R. et al. Sound attenuation by sculpture. *Nature* **378**, 241–241 (1995).
4. Montero de Espinosa, F. R., Jiménez, E. & Torres, M. Ultrasonic band gap in a periodic two-dimensional composite. *Phys. Rev. Lett.* **80**, 1208–1211 (1998).
5. Lu, L., Joannopoulos, J. D. & Soljačić, M. Topological photonics. *Nat. Photon.* **8**, 821–829 (2014).
6. Pancharatnam, S. Generalized theory of interference and its applications. *Proc. Natl. Acad. Sci. India A* **44**, 398–417 (1956).
7. Berry, M. V. Quantal phase factors accompanying adiabatic changes. *Proc. R Soc. Lond. A* **392**, 45–57 (1984).
8. von Bergmann, J. & von Bergmann, H. Foucault pendulum through basic geometry. *Am. J. Phys.* **75**, 888–892 (2007).
9. Tomita, A. & Chiao, R. Y. Observation of Berry’s topological phase by use of an optical fiber. *Phys. Rev. Lett.* **57**, 937–940 (1986).
10. Boulanger, J., Le Bihan, N., Catheline, S. & Rossetto, V. Observation of a non-adiabatic geometric phase for elastic waves. *Ann. Phys.* **327**, 952–958 (2012).
11. Wang, S., Ma, G. & Chan, C. T. Topological transport of sound mediated by spin-redirection geometric phase. *Sci. Adv.* **4**, eaq1475 (2018).
12. Heeger, A. J., Kivelson, S., Schrieffer, J. R. & Su, W. P. Solitons in conducting polymers. *Rev. Mod. Phys.* **60**, 781–850 (1988).
13. Xiao, Y., Ma, G., Zhang, Z.-Q. & Chan, C. T. Topological subspace induced bound states in continuum. *Phys. Rev. Lett.* **118**, 166803 (2017).
14. Zak, J. Berry’s phase for energy bands in solids. *Phys. Rev. Lett.* **62**, 2747–2750 (1989).
15. Xiao, M., Zhang, Z. Q. & Chan, C. T. Surface impedance and bulk band geometric phases in one-dimensional systems. *Phys. Rev. X* **4**, 021017 (2014).
16. Gao, W. et al. Controlling interface states in 1D photonic crystals by tuning bulk geometric phases. *Opt. Lett.* **42**, 1500–1503 (2017).
17. Choi, K. H., Ling, C. W., Lee, K. F., Tsang, Y. H. & Fung, K. H. Simultaneous multi-frequency topological edge modes between one-dimensional photonic crystals. *Opt. Lett.* **41**, 1644–1647 (2016).
18. Yan, M. et al. Designing topological interface states in phononic crystals based on the full phase diagrams. *New J. Phys.* **20**, 073032 (2018).
19. Xiao, M. et al. Geometric phase and band inversion in periodic acoustic systems. *Nat. Phys.* **11**, 240–244 (2015).
This paper reports the first observation of the Zak phase and topological transition in a phononic crystal.
20. Chaunsali, R., Kim, E., Thakkar, A., Kevrekidis, P. G. & Yang, J. Demonstrating an In Situ topological band transition in cylindrical granular chains. *Phys. Rev. Lett.* **119**, 024301 (2017).
21. Yin, J. et al. Band transition and topological interface modes in 1D elastic phononic crystals. *Sci. Rep.* **8**, 6806 (2018).
22. Esmann, M. et al. Topological nanophononic states by band inversion. *Phys. Rev. B* **97**, 155422 (2018).
23. Huang, X., Xiao, M., Zhang, Z.-Q. & Chan, C. T. Sufficient condition for the existence of interface states in some two-dimensional photonic crystals. *Phys. Rev. B* **90**, 075423 (2014).
24. Li, S., Zhao, D., Niu, H., Zhu, X. & Zang, J. Observation of elastic topological states in soft materials. *Nat. Commun.* **9**, 1370 (2018).
25. Delplace, P., Ullmo, D. & Montambaux, G. Zak phase and the existence of edge states in graphene. *Phys. Rev. B* **84**, 195452 (2011).
26. Castro Neto, A. H., Guinea, F., Peres, N. M. R., Novoselov, K. S. & Geim, A. K. The electronic properties of graphene. *Rev. Mod. Phys.* **81**, 109–162 (2009).
27. Hikami, S., Larkin, A. I. & Nagaoka, Y. Spin-Orbit interaction and magnetoresistance in the two dimensional random system. *Prog. Theor. Phys.* **63**, 707–710 (1980).
28. Liu, F., Ming, P. & Li, J. Ab initio calculation of ideal strength and phonon instability of graphene under tension. *Phys. Rev. B* **76**, 064120 (2007).
29. Guinea, F., Katsnelson, M. I. & Geim, A. K. Energy gaps and a zero-field quantum Hall effect in graphene by strain engineering. *Nat. Phys.* **6**, 30 (2009).
30. Wen, X. et al. Observation of acoustic Landau quantization and quantum-Hall-like edge states. Preprint at arXiv <https://arxiv.org/abs/1807.08454v1> (2018).
31. Rechtsman, M. C. et al. Strain-induced pseudomagnetic field and photonic Landau levels in dielectric structures. *Nat. Photon.* **7**, 153–158 (2013).
32. Yang, Z., Gao, F., Yang, Y. & Zhang, B. Strain-induced gauge field and Landau levels in acoustic structures. *Phys. Rev. Lett.* **118**, 194301 (2017).
33. Sepkhanov, R. A., Bazaliy, Y. B. & Beenakker, C. W. J. Extremal transmission at the Dirac point of a photonic band structure. *Phys. Rev. A* **75**, 063813 (2007).
34. Zhang, X. & Liu, Z. Extremal transmission and beating effect of acoustic waves in two-dimensional sonic crystals. *Phys. Rev. Lett.* **101**, 264303 (2008).
35. Torrent, D. & Sánchez-Dehesa, J. Acoustic analogue of graphene: observation of Dirac cones in acoustic surface waves. *Phys. Rev. Lett.* **108**, 174301 (2012).
36. Lu, J. et al. Dirac cones in two-dimensional artificial crystals for classical waves. *Phys. Rev. B* **89**, 134302 (2014).
37. Yu, S.-Y. et al. Surface phononic graphene. *Nat. Mater.* **15**, 1243 (2016).
38. Zhong, W. & Zhang, X. Acoustic analog of monolayer graphene and edge states. *Phys. Lett. A* **375**, 3533–3536 (2011).
39. Dai, H., Xia, B. & Yu, D. Dirac cones in two-dimensional acoustic metamaterials. *J. Appl. Phys.* **122**, 065103 (2017).
40. Torrent, D., Mayou, D. & Sánchez-Dehesa, J. Elastic analogue of graphene: Dirac cones and edge states for flexural waves in thin plates. *Phys. Rev. B* **87**, 115143 (2013).
41. Joshua, E. S. S., Tom, C. L. & Charles, L. K. Mechanical graphene. *New J. Phys.* **19**, 025003 (2017).
42. Chong, C., Kevrekidis, P. G., Ablowitz, M. J. & Ma, Y.-P. Conical wave propagation and diffraction in two-dimensional hexagonally packed granular lattices. *Phys. Rev. E* **93**, 012909 (2016).
43. Thouless, D. J., Kohmoto, M., Nightingale, M. P. & den Nijs, M. Quantized Hall conductance in a two-dimensional periodic potential. *Phys. Rev. Lett.* **49**, 405–408 (1982).
44. Zhang, Y., Tan, Y.-W., Stormer, H. L. & Kim, P. Experimental observation of the quantum Hall effect and Berry’s phase in graphene. *Nature* **438**, 201 (2005).
45. Novoselov, K. S. et al. Room-temperature quantum Hall effect in graphene. *Science* **315**, 1379–1379 (2007).
46. Haldane, F. D. M. & Raghu, S. Possible realization of directional optical waveguides in photonic crystals with broken time-reversal symmetry. *Phys. Rev. Lett.* **100**, 013904 (2008).
47. Klitzing, K. v., Dorda, G. & Pepper, M. New method for high-accuracy determination of the fine-structure constant based on quantized Hall resistance. *Phys. Rev. Lett.* **45**, 494–497 (1980).
48. Wang, Z., Chong, Y., Joannopoulos, J. D. & Soljačić, M. Observation of unidirectional backscattering-immune topological electromagnetic states. *Nature* **461**, 772–775 (2009).
49. Roux, P., de Rosny, J., Tanter, M. & Fink, M. The Aharonov-Bohm effect revisited by an acoustic time-reversal mirror. *Phys. Rev. Lett.* **79**, 3170 (1997).
50. Fleury, R., Sounas, D. L., Sieck, C. F., Haberman, M. R. & Alù, A. Sound isolation and giant linear nonreciprocity in a compact acoustic circulator. *Science* **343**, 516–519 (2014).
51. Yang, Z. et al. Topological acoustics. *Phys. Rev. Lett.* **114**, 114301 (2015).
52. Ni, X. et al. Topologically protected one-way edge mode in networks of acoustic resonators with circulating air flow. *New J. Phys.* **17**, 053016 (2015).
53. Khanikaev, A. B., Fleury, R., Mousavi, S. H. & Alu, A. Topologically robust sound propagation in an angular-momentum-biased graphene-like resonator lattice. *Nat. Commun.* **6**, 8260 (2015).
Together with Yang et al. (2015) and Ni et al. (2015), this paper proposes using circulation of a fluid to break time-reversal symmetry to realize the quantum Hall effect in sound.
54. Souslov, A., van Zuiden, B. C., Bartolo, D. & Vitelli, V. Topological sound in active-liquid metamaterials. *Nat. Phys.* **13**, 1091–1094 (2017).
55. Hatsugai, Y. Chern number and edge states in the integer quantum Hall effect. *Phys. Rev. Lett.* **71**, 3697–3700 (1993).
56. Kane, C. L. & Mele, E. J. Z2 Topological order and the quantum spin hall effect. *Phys. Rev. Lett.* **95**, 146802 (2005).
57. Chen, Z.-G. & Wu, Y. Tunable topological phononic crystals. *Phys. Rev. Appl.* **5**, 054021 (2016).
58. Zhu, Y. et al. Experimental realization of acoustic chern insulator. *Phys. Rev. Lett.* **122**, 014302 (2019).
59. Wang, P., Lu, L. & Bertoldi, K. Topological phononic crystals with one-way elastic edge waves. *Phys. Rev. Lett.* **115**, 104302 (2015).
60. Nash, L. M. et al. Topological mechanics of gyroscopic metamaterials. *Proc. Natl. Acad. Sci.* **112**, 14495–14500 (2015).
This work uses electric motors to break time-reversal symmetry to realize a mechanical Chern insulator.
61. Yao-Ting, W., Pi-Gang, L. & Shuang, Z. Coriolis force induced topological order for classical mechanical vibrations. *New J. Phys.* **17**, 073031 (2015).
62. Kane, C. L. & Mele, E. J. Quantum spin Hall effect in graphene. *Phys. Rev. Lett.* **95**, 226801 (2005).
63. Bernevig, B. A., Hughes, T. L. & Zhang, S.-C. Quantum spin Hall effect and topological phase transition in HgTe quantum wells. *Science* **314**, 1757–1761 (2006).
64. König, M. et al. Quantum spin Hall insulator state in HgTe quantum wells. *Science* **318**, 766 (2007).
65. Süssstrunk, R. & Huber, S. D. Observation of phononic helical edge states in a mechanical topological insulator. *Science* **349**, 47–50 (2015).
This is the first realization of the analogy of the QSH effect in a mechanical system.
66. Hofstadter, D. R. Energy levels and wave functions of Bloch electrons in rational and irrational magnetic fields. *Phys. Rev. B* **14**, 2239–2249 (1976).
67. He, C. et al. Acoustic topological insulator and robust one-way sound transport. *Nat. Phys.* **12**, 1124–1129 (2016).
This is the first experimental realization of a 2D topological insulator for sound.
68. Wu, L.-H. & Hu, X. Scheme for achieving a topological photonic crystal by using dielectric material. *Phys. Rev. Lett.* **114**, 223901 (2015).
69. Zhang, Z. et al. Topological creation of acoustic pseudospin multipoles in a flow-free symmetry-broken metamaterial lattice. *Phys. Rev. Lett.* **118**, 084303 (2017).

70. Simon, Y., Romain, F., Fabrice, L., Mathias, F. & Geoffroy, L. Topological acoustic polaritons: robust sound manipulation at the subwavelength scale. *New J. Phys.* **19**, 075003 (2017).
71. Hafezi, M., Demler, E. A., Lukin, M. D. & Taylor, J. M. Robust optical delay lines with topological protection. *Nat. Phys.* **7**, 907–912 (2011).
72. Liang, G. Q. & Chong, Y. D. Optical resonator analog of a two-dimensional topological insulator. *Phys. Rev. Lett.* **110**, 203904 (2013).
73. Peng, Y.-G. et al. Experimental demonstration of anomalous Floquet topological insulator for sound. *Nat. Commun.* **7**, 13368 (2016).
74. Li, J., Wang, J., Wu, S. & Mei, J. Pseudospins and topological edge states in elastic shear waves. *AIP Adv.* **7**, 125030 (2017).
75. Shiqiao, W., Ying, W. & Jun, M. Topological helical edge states in water waves over a topographical bottom. *New J. Phys.* **20**, 023051 (2018).
76. Yu, S.-Y. et al. Elastic pseudospin transport for integrable topological phononic circuits. *Nat. Commun.* **9**, 3072 (2018).
77. Mousavi, S. H., Khanikaev, A. B. & Wang, Z. Topologically protected elastic waves in phononic metamaterials. *Nat. Commun.* **6**, 8682 (2015).
78. Miniaci, M., Pal, R. K., Morvan, B. & Ruzzene, M. Experimental observation of topologically protected helical edge modes in patterned elastic plates. *Phys. Rev. X* **8**, 031074 (2018).
79. Zheng, L.-Y., Theocharis, G., Tournat, V. & Gusev, V. Quasitopological rotational waves in mechanical granular graphene. *Phys. Rev. B* **97**, 060101 (2018).
80. Lu, J., Oiu, C., Ke, M. & Liu, Z. Valley vortex states in sonic crystals. *Phys. Rev. Lett.* **116**, 093901 (2016).
81. Lu, J. et al. Observation of topological valley transport of sound in sonic crystals. *Nat. Phys.* **13**, 364–374 (2016).
This paper reports the realization of the valley Hall effect in phononic crystals.
82. Ye, L. et al. Observation of acoustic valley vortex states and valley-chirality locked beam splitting. *Phys. Rev. B* **95**, 174106 (2017).
83. Lu, J. et al. Valley topological phases in bilayer sonic crystals. *Phys. Rev. Lett.* **120**, 116802 (2018).
84. Xia, B.-Z. et al. Observation of valleylike edge states of sound at a momentum away from the high-symmetry points. *Phys. Rev. B* **97**, 155124 (2018).
85. Zhang, Z. et al. Topological acoustic delay line. *Phys. Rev. Appl.* **9**, 034032 (2018).
86. Yang, Y., Yang, Z. & Zhang, B. Acoustic valley edge states in a graphene-like resonator system. *J. Appl. Phys.* **123**, 091713 (2018).
87. Yan, M. et al. On-chip valley topological materials for elastic wave manipulation. *Nat. Mater.* **17**, 993–998 (2018).
88. Liu, T.-W. & Semperlotti, F. Tunable acoustic valley hall edge states in reconfigurable phononic elastic waveguides. *Phys. Rev. Appl.* **9**, 014001 (2018).
89. Kitagawa, T., Berg, E., Rudner, M. & Demler, E. Topological characterization of periodically driven quantum systems. *Phys. Rev. B* **82**, 235114 (2010).
90. Fleury, R., Khanikaev, A. B. & Alu, A. Floquet topological insulators for sound. *Nat. Commun.* **7**, 11744 (2016).
This is a theoretical and numerical study of a Floquet topological insulator for sound.
91. Rechtsman, M. C. et al. Photonic Floquet topological insulators. *Nature* **496**, 196–200 (2013).
92. Peng, Y.-G., Geng, Z.-G. & Zhu, X.-F. Topologically protected bound states in one-dimensional Floquet acoustic waveguide systems. *J. Appl. Phys.* **123**, 091716 (2018).
93. Pasek, M. & Chong, Y. D. Network models of photonic Floquet topological insulators. *Phys. Rev. B* **89**, 075113 (2014).
94. Hermann, W. *Elektron und Gravitation. I* [German]. *Z. für Phys.* **56**, 330–352 (1929).
95. Xiao, M., Chen, W.-J., He, W.-Y. & Chan, C. T. Synthetic gauge flux and Weyl points in acoustic systems. *Nat. Phys.* **11**, 920–924 (2015).
This paper discusses how to realize Weyl points in phononic crystals.
96. Chang, M.-L., Xiao, M., Chen, W.-J. & Chan, C. T. Multiple Weyl points and the sign change of their topological charges in woodpile photonic crystals. *Phys. Rev. B* **95**, 125136 (2017).
97. He, H. et al. Topological negative refraction of surface acoustic waves in a Weyl phononic crystal. *Nature* **560**, 61–64 (2018).
98. Liu, T., Zheng, S., Dai, H., Yu, D. & Xia, B. Acoustic semimetal with Weyl points and surface states. Preprint at arXiv <https://arxiv.org/abs/1803.04284> (2018).
99. Li, F., Huang, X., Lu, J., Ma, J. & Liu, Z. Weyl points and Fermi arcs in a chiral phononic crystal. *Nat. Phys.* **14**, 30–34 (2018).
This is the first experimental realization of acoustic Weyl points.
100. Ge, H. et al. Experimental observation of acoustic Weyl points and topological surface states. *Phys. Rev. Appl.* **10**, 014017 (2018).
101. Soluyanov, A. A. et al. Type-II Weyl semimetals. *Nature* **527**, 495–498 (2015).
102. Yang, Z. & Zhang, B. Acoustic type-II Weyl nodes from stacking dimerized chains. *Phys. Rev. Lett.* **117**, 224301 (2016).
103. Fruchart, M. et al. Soft self-assembly of Weyl materials for light and sound. *Proc. Natl. Acad. Sci. USA* **115**, E3655 (2018).
104. Yao-Ting, W. & Ya-Wen, T. Multiple Weyl and double-Weyl points in an elastic chiral lattice. *New J. Phys.* **20**, 083031 (2018).
105. Fang, C., Gilbert, M. J., Dai, X. & Bernevig, B. A. Multi-Weyl topological semimetals stabilized by point group symmetry. *Phys. Rev. Lett.* **108**, 266802 (2012).
106. Chen, W.-J., Xiao, M. & Chan, C. T. Photonic crystals possessing multiple Weyl points and the experimental observation of robust surface states. *Nat. Commun.* **7**, 13038 (2016).
107. Zhang, T. et al. Double-Weyl phonons in transition-metal monosilicides. *Phys. Rev. Lett.* **120**, 016401 (2018).
108. Xiao, M. & Fan, S. Topologically charged nodal surface. Preprint at arXiv <https://arxiv.org/abs/1709.02363> (2017).
109. Liu, Z. K. et al. Discovery of a three-dimensional topological Dirac semimetal, Na₃Bi. *Science* **343**, 864–867 (2014).
110. Kane, C. L. & Lubensky, T. C. Topological boundary modes in isotactic lattices. *Nat. Phys.* **10**, 39–45 (2014).
111. Rocklin, D. Z., Chen, B. Gg, Falk, M., Vitelli, V. & Lubensky, T. C. Mechanical Weyl modes in topological Maxwell lattices. *Phys. Rev. Lett.* **116**, 135503 (2016).
112. Paulose, J., Meussen, A. S. & Vitelli, V. Selective buckling via states of self-stress in topological metamaterials. *Proc. Natl. Acad. Sci. USA* **112**, 7639–7644 (2015).
113. Meussen, A. S., Paulose, J. & Vitelli, V. Geared topological metamaterials with tunable mechanical stability. *Phys. Rev. X* **6**, 041029 (2016).
114. Huber, S. D. Topological mechanics. *Nat. Phys.* **12**, 621 (2016).
115. Bertoldi, K., Vitelli, V., Christensen, J. & van Hecke, M. Flexible mechanical metamaterials. *Nat. Rev. Mater.* **2**, 17066 (2017).
116. Benalcazar, W. A., Bernevig, B. A. & Hughes, T. L. Quantized electric multipole insulators. *Science* **357**, 61–66 (2017).
117. Serra-Garcia, M. et al. Observation of a phononic quadrupole topological insulator. *Nature* **555**, 342–345 (2018).
118. Xue, H., Yang, Y., Gao, F., Chong, Y. & Zhang, B. Acoustic higher-order topological insulator on a kagome lattice. *Nat. Mater.* **18**, 108–112 (2018).
119. Ni, X., Weiner, M., Alù, A. & Khanikaev, A. B. Observation of higher-order topological acoustic states protected by generalized chiral symmetry. *Nat. Mater.* **18**, 113–120 (2018).
120. Zhang, X. et al. Acoustic hierarchical topological insulators. Preprint at arXiv <https://arxiv.org/abs/1811.05514> (2018).
121. Mitchell, N. P., Nash, L. M., Hexner, D., Turner, A. M. & Irvine, W. T. M. Amorphous topological insulators constructed from random point sets. *Nat. Phys.* **14**, 380–385 (2018).
122. Fu, L., Kane, C. L. & Mele, E. J. Topological insulators in three dimensions. *Phys. Rev. Lett.* **98**, 106803 (2007).
123. Yang, Y. et al. Realization of a three-dimensional photonic topological insulator. *Nature* **565**, 622–626, doi: (2019).
124. Li, J., Chu, R.-L., Jain, J. K. & Shen, S.-Q. Topological anderson insulator. *Phys. Rev. Lett.* **102**, 136806 (2009).
125. Stützer, S. et al. Photonic topological Anderson insulators. *Nature* **560**, 461 (2018).
126. Aubry, S. & André, G. Analyticity breaking and anderson localization in incommensurate lattices. *Ann. Isr. Phys. Soc.* **3**, 18 (1980).
127. Zhu, W. et al. Simultaneous observation of a topological edge state and exceptional point in an open and non-hermitian acoustic system. *Phys. Rev. Lett.* **121**, 124501 (2018).
128. Kitaev, A. Y. Unpaired Majorana fermions in quantum wires. *Sov. Phys. Usp.* **44**, 131 (2001).
129. El-Ganainy, R. et al. Non-Hermitian physics and PT-symmetry. *Nat. Phys.* **14**, 11 (2018).
130. Feng, L., El-Ganainy, R. & Ge, L. Non-Hermitian photonics based on parity-time symmetry. *Nat. Photon.* **11**, 752–762 (2017).
131. Leykam, D. & Chong, Y. D. Edge solitons in nonlinear-photonic topological insulators. *Phys. Rev. Lett.* **117**, 143901 (2016).
132. Li, G., Zhang, S. & Zentgraf, T. Nonlinear photonic metasurfaces. *Nat. Rev. Mater.* **2**, 17010 (2017).
133. Fang, A., Zhang, Z. Q., Louie, S. G. & Chan, C. T. Anomalous Anderson localization behaviors in disordered pseudospin systems. *Proc. Natl. Acad. Sci. USA* **114**, 4087–4092 (2017).
134. Chan, C. T., Hang, Z. H. & Huang, X. Dirac dispersion in two-dimensional photonic crystals. *Adv. Optoelectron.* **2012**, 11 (2012).
135. Liu, F., Huang, X. & Chan, C. T. Dirac cones at *k* in acoustic crystals and zero refractive index acoustic materials. *Appl. Phys. Lett.* **100**, 071911–071914 (2012).
136. Huang, X., Lai, Y., Hang, Z. H., Zheng, H. & Chan, C. T. Dirac cones induced by accidental degeneracy in photonic crystals and zero-refractive-index materials. *Nat. Mater.* **10**, 582–586 (2011).
137. Mei, J., Wu, Y., Chan, C. T. & Zhang, Z.-Q. First-principles study of Dirac and Dirac-like cones in phononic and photonic crystals. *Phys. Rev. B* **86**, 035141 (2012).
138. Dubois, M., Shi, C., Zhu, X., Wang, Y. & Zhang, X. Observation of acoustic Dirac-like cone and double zero refractive index. *Nat. Commun.* **8**, 14871 (2017).
139. Liu, F. & Liu, Z. Elastic waves scattering without conversion in metamaterials with simultaneous zero indices for longitudinal and transverse waves. *Phys. Rev. Lett.* **115**, 175502 (2015).
140. Chan, C. T., Huang, X., Liu, F. & Hang, Z. H. Dirac dispersion and zero-index in two dimensional and three dimensional photonic and phononic systems. *Prog. Electromagn. Res. B* **44**, 163–190 (2012).
141. Liu, F., Lai, Y., Huang, X. & Chan, C. T. Dirac cones at *k*=0 in phononic crystals. *Phys. Rev. B* **84**, 224113 (2011).
142. Huang, X., Xiao, M., Chan, C. T. & Liu, F. in *World Scientific Handbook of Metamaterials and Plasmonics World Scientific Series in Nanoscience and Nanotechnology* 553–597 (World Scientific, 2017).
143. Wu, Y. A semi-Dirac point and an electromagnetic topological transition in a dielectric photonic crystal. *Opt. Express* **22**, 1906–1917 (2014).
144. Sakoda, K. Proof of the universality of mode symmetries in creating photonic Dirac cones. *Opt. Express* **20**, 25181–25194 (2012).
145. Li, Y., Wu, Y. & Mei, J. Double Dirac cones in phononic crystals. *Appl. Phys. Lett.* **105**, 014107 (2014).
146. Chen, Z.-G. et al. Accidental degeneracy of double Dirac cones in a phononic crystal. *Sci. Rep.* **4**, 4613 (2014).
147. Zhou, X. et al. Photonic spin Hall effect in topological insulators. *Phys. Rev. A* **88**, 053840 (2013).

Acknowledgements

The authors are grateful to R.-Y. Zhang for proofreading the manuscript. G.M. thanks W.-J. Chen, Shubo Wang and Changqing Xu for helpful discussions. G.M. is supported by the Hong Kong Research Grants Council (grant no. RGC-ECS 22302718, ANR-RGC A-HKUST601/18 and CRF C6013-18GF), the National Natural Science Foundation of China (grant no. 11802256) and the Hong Kong Baptist University through FRG2/17-18/056. M.X. is supported by the startup funding of Wuhan University and the US National Science Foundation (grant no. CBET-1641069). C.T.C. is supported by the Hong Kong Research Grants Council (grant no. AoE/P-02/12).

Author contributions

All authors contributed to the writing of the manuscript.

Competing interests

The authors declare no competing interests.

Publisher's note

Springer Nature remains neutral with regard to jurisdictional claims in published maps and institutional affiliations.